



**HAL**  
open science

# Numerical analysis of cross-sectional effects during the magnetic pulse disassembly of laminate structures

Benoit Lagain, Thomas Heuzé, Guillaume Racineux, M. Arrigoni

## ► To cite this version:

Benoit Lagain, Thomas Heuzé, Guillaume Racineux, M. Arrigoni. Numerical analysis of cross-sectional effects during the magnetic pulse disassembly of laminate structures. *Advanced Engineering Materials*, 2023, 10.1002/adem.202300728 . hal-04180423

**HAL Id: hal-04180423**

**<https://hal.science/hal-04180423>**

Submitted on 27 May 2024

**HAL** is a multi-disciplinary open access archive for the deposit and dissemination of scientific research documents, whether they are published or not. The documents may come from teaching and research institutions in France or abroad, or from public or private research centers.

L'archive ouverte pluridisciplinaire **HAL**, est destinée au dépôt et à la diffusion de documents scientifiques de niveau recherche, publiés ou non, émanant des établissements d'enseignement et de recherche français ou étrangers, des laboratoires publics ou privés.



Distributed under a Creative Commons Attribution - NonCommercial - NoDerivatives 4.0 International License

# Numerical Analysis of Cross-Sectional Effects During the Magnetic Pulse Disassembly of Laminate Structures

Benoit Lagain,\* Thomas Heuzé, Guillaume Racineux, and Michel Arrigoni

To improve the performances of engineered systems, laminate composite structures are widely used as they offer the best strength-to-weight ratio. However, maintenance and recycling of these structures still remain a challenge. One solution can be to disassemble the layers, without damaging them, so that they can be repaired, reused, or recycled. To do so, impulsive sources such as high pulsed powers are considered. Herein, the influence of transverse or cross-sectional effects on the wave propagation within the laminate and on its disassembly conditions is studied by means of two-dimensional numerical simulations performed on a model assembly using the finite element method. The specimen considered is an aluminum/steel assembly joined along a stripe. Two different modelings of the loading applied to the laminate of increasing complexity are successively considered. First, linear elastodynamic simulations show that transverse effects reduce by around 12% the maximum achievable interfacial tensile stress ratio compared with that predicted by the 1D reference model. Then, weakly coupled eddy current-linear elastodynamic numerical analyses clarify the latter result with an estimation of about 16% with respect to the 1D analytical solution. These results permit the design of experiments serving as a proof of concept of the proposed process.

## 1. Introduction

To improve the performance of industrial components, it is important to develop structures with the best strength-to-weight ratio. Hence, composite structures, and especially laminated structures, are increasingly used in many fields such as aeronautics, space exploration, or ballistic protection. Most of these

structures are made up of layers of different materials. Because of their heterogeneity, the recycling of laminates remains a challenge. One solution could be to disassemble the layers so that they can be reused or recycled independently of each other.

An open question is how to disassemble them without damaging the other layers. In this context, dynamic effects can be profitably considered to perform the disassembly. Indeed, dynamics effects have already been used for the measurement of the bond strength of composite structures, for which various testing methods were developed in the past years.<sup>[1–5]</sup> The purpose of these methods is mostly to create a mechanical wave inside a structure to test the mechanical strength of the interface.<sup>[6–10]</sup> Among these methods, the ARCAN test can be mentioned.<sup>[11–15]</sup> Despite its ability to weigh tension/compression and shear loadings when testing the bond strength, the ARCAN test remains a laboratory method. To answer the aforementioned issue, shock adhesion tests were developed.<sup>[1,5,16]</sup> Some


of them are contactless like the LASer Shock Adhesion Testing (LASAT), which consists of a rapid diagnostic process based on laser Doppler velocimetry.<sup>[2,4]</sup> The LASAT method can also be used as a composite delaminator on a variety of composite materials.<sup>[17,18]</sup> However, the short duration of the pulse and its sensitivity to spot size, which makes the technique dependent on edge effects, limit its application to composites and assemblies with a thickness lying between 0.8 and 3 mm.<sup>[19,20]</sup>

To overcome these limitations, the magnetic pulse technology can be used to process thicker structures, as its characteristic loading time is much longer than that of a laser pulse. It has already been used to assemble structures, using magnetic pulse welding,<sup>[21–26]</sup> or to form various geometries of sheets or shells, thanks to the magnetic pulse forming.<sup>[27–30]</sup> Some attempts to disassemble adhesively bonded composite materials were also reported.<sup>[20]</sup> The purpose of these technologies is to discharge into an inductor and in a short time a given quantity of electrical energy previously stored in a capacitor bank and to exploit Lorentz forces generated in neighboring electrical conductors to propagate mechanical waves inside the structure of interest.

The feasibility of using high-powered pulses to disassemble laminate structures was demonstrated in a previous study,<sup>[31]</sup> in which optimal disassembly conditions were obtained analytically from the solution of an optimization problem involving simplified one-dimensional modeling, hence only considering plane

B. Lagain, T. Heuzé, G. Racineux  
Research Institute in Civil and Mechanical Engineering (GeM)  
UMR 6183 CNRS) Ecole Centrale de Nantes  
1 rue de la Noë, F-44321 Nantes, France  
E-mail: benoit.lagain@ec-nantes.fr

M. Arrigoni  
ENSTA Bretagne, Institut de recherche Dupuy de Lôme (IRD L)  
UMR CNRS 6027  
29806 Brest, France

 The ORCID identification number(s) for the author(s) of this article can be found under <https://doi.org/10.1002/adem.202300728>.

© 2023 The Authors. Advanced Engineering Materials published by Wiley-VCH GmbH. This is an open access article under the terms of the Creative Commons Attribution-NonCommercial-NoDerivs License, which permits use and distribution in any medium, provided the original work is properly cited, the use is non-commercial and no modifications or adaptations are made.

DOI: 10.1002/adem.202300728

waves. The present article proposes to improve the design of the magnetic pulse disassembly method by studying the influence of transverse or cross-sectional effects on the wave propagation inside the laminate, that is considering that propagating waves are actually not plane waves, and on its disassembly conditions. The optimization problem considered in the study of Lagain et al.<sup>[31]</sup> can therefore be seen as a simplification of a more general problem. In the latter, the cross-sectional effects are considered, so that the cross-sectional lengths and thicknesses of the laminate layers are part of the unknowns in the optimization problem. In the present approach, a two-dimensional analysis based on the finite element method proposes numerical simulations of increasing complexity to study the impact of cross-sectional effects during the magnetic pulse disassembly of a two-layered laminate structure, whose configurations were pre-selected from the 1D analytical results.<sup>[31]</sup>

The outline of the present article is as follows. Section 1 presents the simplified two-dimensional modeling of the laminate, the optimization problem whose objective is to disassemble the laminate, and the following methods of analysis. Especially, numerical simulations are performed with the finite element software COMSOL Multiphysics.<sup>[32]</sup> Section 2 presents the numerical results obtained in linear elastodynamics, embedding a simplified modeling of the mechanical loading. Section 3 shows results obtained with a weakly coupled eddy current-linear elastodynamic analysis. Such coupling enables a more accurate computation of the mechanical pulse resulting from the generated Lorentz forces. Finally, a comparison between both modelings allows a discussion on the importance of accounting for such coupling in simulations about the definition of the optimal conditions for disassembling the laminate.

## 2. Modeling and Methodology

### 2.1. Two-Dimensional Simplified Modeling

A two-layered laminate structure of geometry extruded along the direction  $z$  is considered, assembled through a centered band of width  $2l_{\text{joint}}$ , as shown in Figure 1. It is assumed that the thickness of the joint  $d_{\text{joint}}$  in the direction  $y$  is far lower than those of layers A and B, i.e.,  $d_{\text{joint}} \ll \min(d_A, d_B)$ . Therefore, various technologies can be considered to assemble the laminate provided the aforementioned condition is satisfied, such as

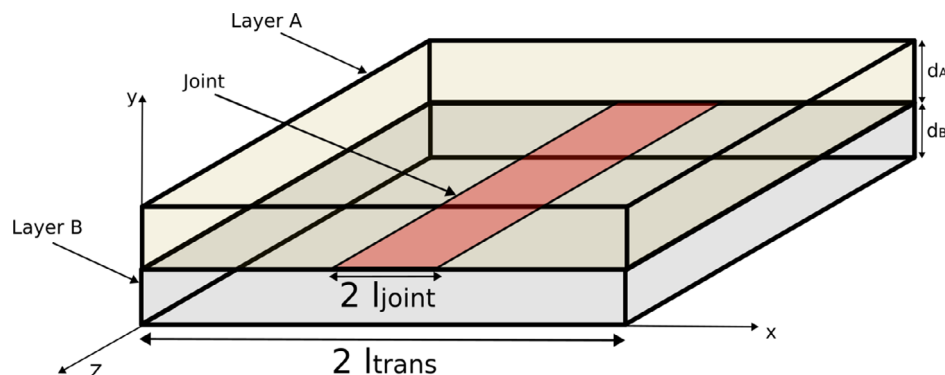


**Figure 1.** Two-layered laminate structure assembled by a bond strip.

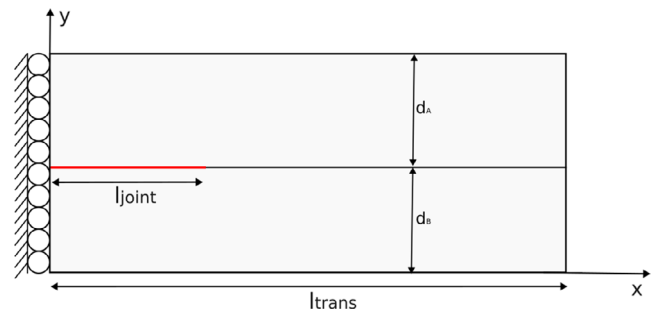


**Figure 2.** Simplified two-dimensional modeling of a two-layered laminate structure.

adhesive bonding, magnetic pulse welding or any other surface joining methods and additive methods such as thermal spraying. Only assembly methods affecting layers in their volumes like arc welding, friction Stir Welding, or others do not enter the present study.

Since the laminate presents a geometry of translation along the direction  $z$ , and considering that the in-plane transversal length  $2l_{\text{trans}}$  of each layer is far lower than the out-of-plane one, it can be modeled at first glance in a two-dimensional setting, with plane strain conditions. Then, the configuration of the laminate shows a symmetry plane (Figure 1) at coordinate  $x = l_{\text{trans}}$ . Hence, a two-dimensional simplified model of half the structure of the laminate is shown in Figure 2. The continuity of the displacement and of the traction vectors is ensured by the joint on the interval  $x \in [0, l_{\text{joint}}]$ , while the remaining interface is traction-free, which can be considered as crack lips. An input pulse is applied on the top of the laminate ( $y = d_A + d_B$ ), distributed on the interval  $x \in [0, l_{\text{load}}]$ , and detailed thereafter. Except for the left symmetry condition, other boundaries are traction-free. To fix ideas, isotropic and known generic materials are considered in this study for the layers A and B, which are model aluminum and steel respectively, whose mechanical properties are gathered in Table 1.

### 2.2. Optimization Problem

The technology of magnetic pulse disassembly aims at disassembling the interface between the layers of a two-layered laminate structure without damaging them. To achieve this, the laminate

**Table 1.** Properties of generic materials considered.

Material	Young's modulus [GPa]	Poisson's ratio	Density [kg m <sup>-3</sup> ]
Aluminum	70	0.33	2,700
Steel	200	0.29	7,870

is subjected to a magnetic pulse applied on a part of its top face, resulting from the discharge within an inductor of some electrical energy stored in a capacitor bank. The oscillating current flowing in the coil generates eddy currents within a skin depth of the first layer of the laminate, which therefore has to be electrically conductive. High repulsive Lorentz body forces resulting from these eddy currents, generate a stress wave that propagates within the laminate and especially through its thickness.

It is worthwhile to recall that, in dynamics, some tensile stress can emerge from the interaction of two release waves. Therefore, for a given magnetic pulse of duration  $\tau$ , it can be envisaged to take advantage of the above-mentioned interaction to induce tensile stress at the interface between the two layers to debond them. Then, the challenge is to maximize the debonding stress by adjusting a set of geometrical parameters of the laminate as well as the material properties of each layer to maximize the efficiency of the process. The same reasoning was already applied in the LASAT test,<sup>[1]</sup> and experienced with magnetic forces on Adhesively bonded composites.<sup>[20]</sup> However, laser-induced shock waves are better suited to test very thin layers of millimeter range, because of their very short characteristic loading time. **Figure 3** shows a Lagrange diagram, where a few characteristic lines are plotted along which pressure waves travel inside the thickness of the laminate when the latter is submitted to a magnetic pulse of duration  $\tau$ . The maximal applied pressure state travels through the thickness of the layer A along the characteristic line 5 – 3, part of which is then propagated till the bottom of the laminate at point 2. Then, two unloading waves cross at point 1, the characteristic line 4 – 1 coming from the unloading at the top

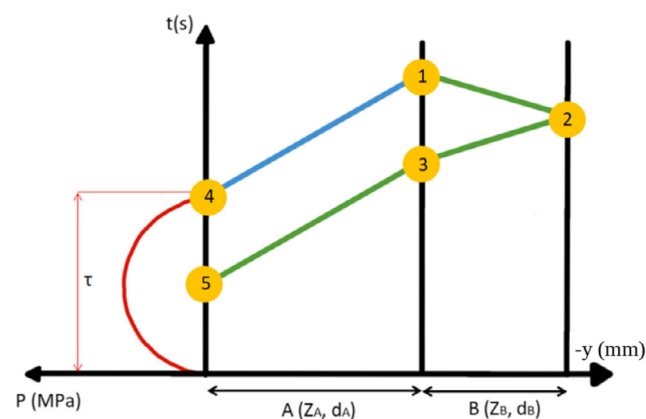


**Figure 3.** Characteristic plane  $(-y, t)$  plotted with two layers (A, B), on which a few characteristics lines are plotted from the unloaded state (in blue) and from the maximum loaded one at the left side of the laminate in the three layers (in green). The interface tensile stress appears at the crossing between the rightward characteristic joining states 4 and 1, and the leftward characteristic joining states 2 and 1. The loading pressure is added on the left part of the ordinate axis.

boundary, and the characteristic line 2 – 1 resulting from the free end at the bottom of the laminate. Therefore, the point 1 is the locus of the occurrence of a normal tensile stress.

Provided a given electric pulse generator delivering some known magnetic pulse, the design of a debondable laminate and therefore of the technology of magnetic pulse disassembly may follow from the solution of an optimization problem whose purpose is to determine an optimal configuration of the laminate which permits to maximize the normal tensile stress at the interface  $\sigma_{yy}^{\text{interface}}(t = T; \mathbf{X}, \mathbf{Y}) \equiv \sigma_{yy}(y = d_B, t = T; \mathbf{X}, \mathbf{Y})$  occurring between the two layers. This optimization problem reads

$$(p_0): \max_{\mathbf{X}} \left( \frac{\sigma_{yy}^{\text{interface}}(t = T; \mathbf{X}, \mathbf{Y})}{P_{\max}} \right) \quad (1)$$

and is carried out with respect to an array of unknown variables  $\mathbf{X}$

$$\mathbf{X} = \{d_A, d_B, Z_A, Z_B, l_{\text{trans}}, T\} \quad (2)$$

that consists of the thicknesses of the two layers, their acoustic impedances  $Z_i$ ,  $i = A, B$ , some transverse length  $l_{\text{trans}}$  in the two-dimensional setting, and the time  $T$  after which the maximum

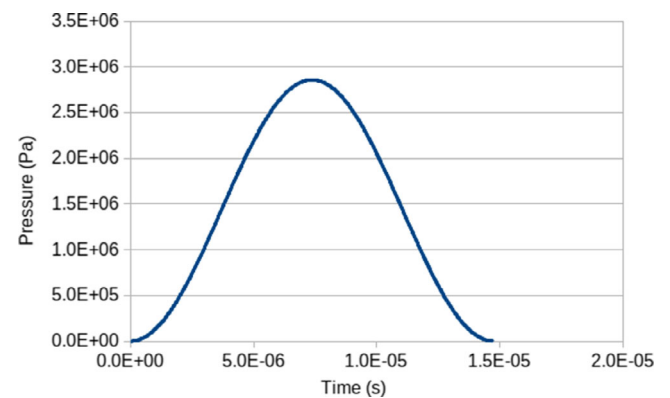


**Figure 4.** Time evolution of the applied pressure in the linear elastodynamic analysis.

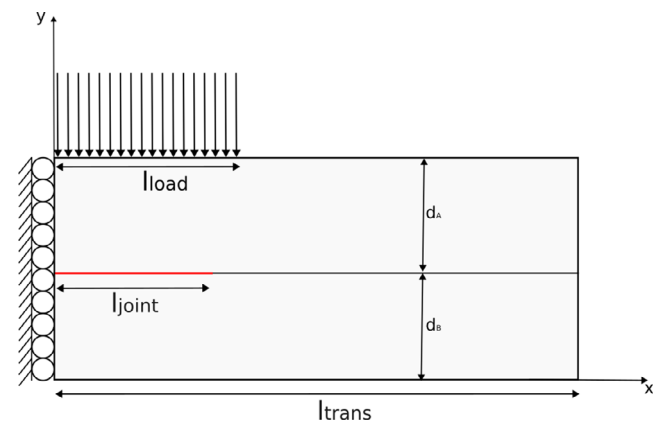


**Figure 5.** Two-layered laminate structure assembled by a bond joint: two-dimensional linear elastodynamic analysis submitted to a uniformly distributed pressure on the subpart  $x \in [0, l_{\text{joint}}]$  of its top face.

interfacial normal stress is reached. Notice that this interfacial tensile stress depends on both the optimization variables  $\mathbf{X}$  and known given quantities  $\mathbf{Y} = \{\bar{P}(t)\}$ , consisting here of the applied loading. Next, the optimization problem is conducted under the obvious constraints

$$\mathbf{X} \in (\mathbb{R}^{+*})^6 \quad (3)$$

It should also be noticed that many failure criteria exist to describe the failure of interfaces.<sup>[33]</sup> However, to avoid to complicate the solution of the optimization problem (1), the study of wave-propagation effects on the generation of stress at the interface is decoupled in the present analysis from that of its kinetics of decohesion, which would require a whole study in itself. Rather, the interfacial failure is assumed to occur in the present study as soon as the interfacial tensile normal stress reaches some known limit stress  $\sigma_r$ . This description is known as “cut-off” pressure. As an example, such “cut-off” stress can be defined as the minimum of the Hugoniot’s elastic limits of both layers, the strength of the interface is considered to be weaker or equal than those of the layers. This is a technological choice allowing to say that the aimed disassembling method remains nondestructive.

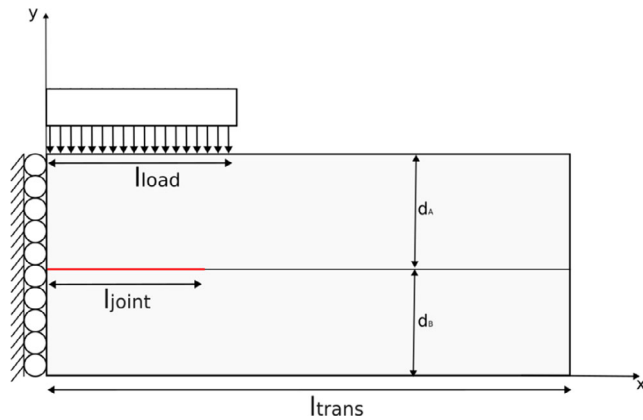


Figure 6. Two-layered laminate structure assembled by a bond joint : two-dimensional eddy current-linear elastodynamic weakly coupled analysis.

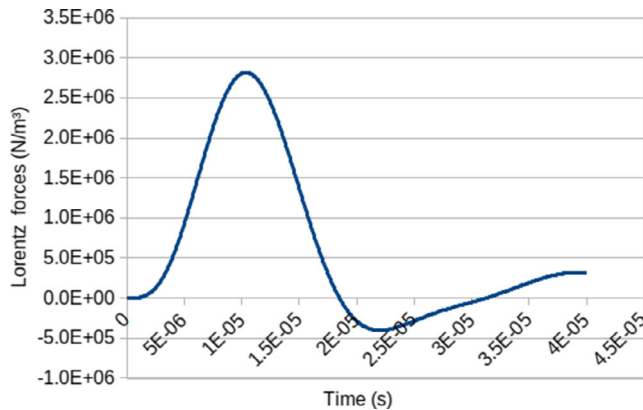


Figure 7. Time evolution of the current density inside the inductor, from Equation (10).

The cost function of the optimization problem (2) can also be seen as some demultiplication factor of the stress, hence qualifying the efficiency of the process, which is expected to be greater or equal to unity. Indeed, thanks to dynamic effects we expect to get a greater normal tensile stress at the interface than the maximum pressure applied on the loaded face of the laminate.

However, the solution to the optimization problem ( $p_0$ ) (1) may be made easier by decoupling the effects of the propagation of waves in the through-thickness and transverse directions of the laminate. As a first step, a previous work<sup>[31]</sup> consisted in introducing an auxiliary optimization problem ( $p_1$ ) with the same cost function than that of the problem ( $p_0$ ) (1), but solved on the reduced array of unknown variables

$$\mathbf{X}_N = \{d_A, d_B, Z_A, Z_B, T\} \quad (4)$$

associated with the through-thickness or “normal” direction of the laminate, under the constraints  $\mathbf{X}_N \in (\mathbb{R}^{+*})^5$ . This auxiliary optimization problem involved a simplified one-dimensional

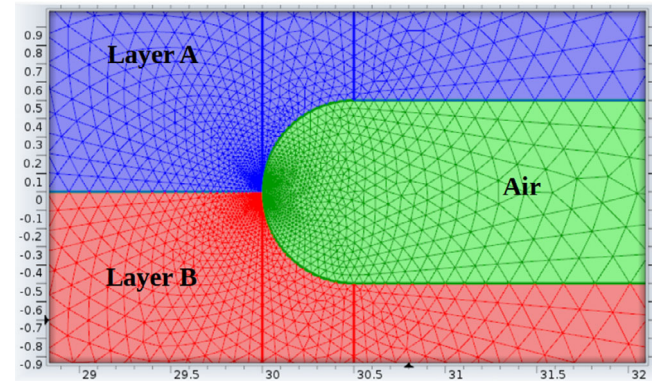


Figure 8. Zoom on the leave of radius  $5 \times 10^{-2}$  mm, located at the right extremity of the joint.

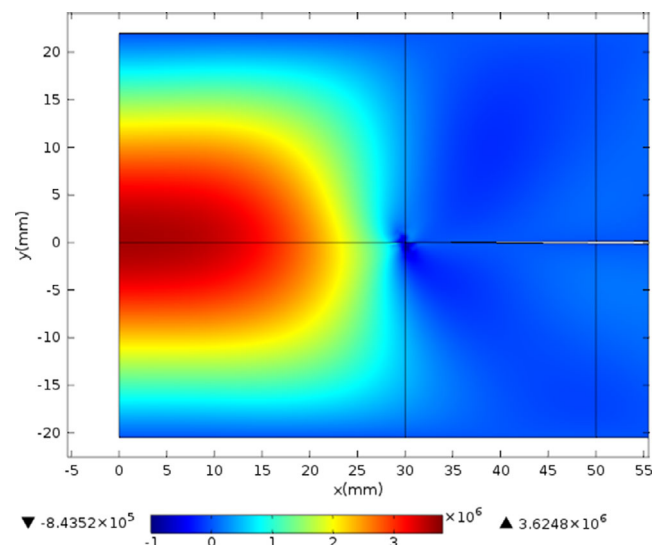


Figure 9. Map of the normal stress component  $\sigma_{yy}$  (in Pa) in the cross-section of the laminate at time  $t = T$ , when computed with the linear elastodynamic analysis.

modeling in linear elastodynamics of the laminate in its through-thickness direction, hence focusing only on pressure waves, disregarding transverse effects and the influence of shear waves. These simplifications allowed us to derive analytical expressions of the debonding stress defined in a piecewise manner according to the instance of the unknown vector  $\mathbf{X}_N$ , and to find various configurations of the laminate that could allow its debonding by magnetic pulse. Among them, the optimal one is given by the conditions

$$d_B = \frac{\tau c_B}{4} \quad (5)$$

$$\frac{d_A}{d_B} = \frac{c_A}{c_B} \quad (6)$$

where  $c_i$ ,  $i = A, B$ , denote the longitudinal sound speed in each layer, and  $\tau$  is the duration of the first half pseudo-period of some square sine pressure signal, see Equation (9). The condition (5) permits to localize the tensile stress at the interface between the two layers at time  $t = \tau + \frac{d_A}{c_A}$ , Equation (6) allows to reach the maximal interfacial tensile stress ratio

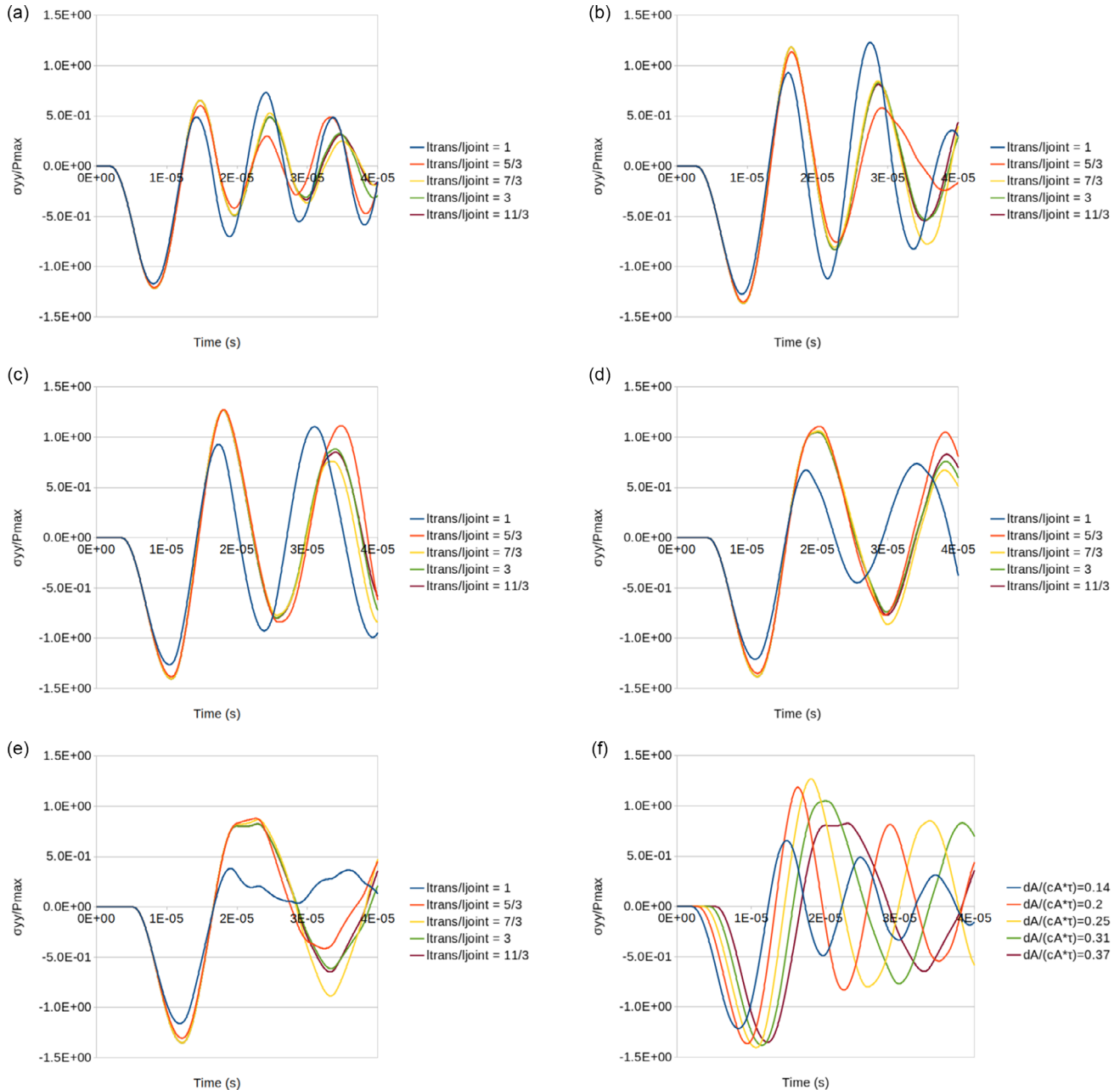


**Figure 10.** Time evolutions of the interfacial stress ratio  $\sigma_{yy}/P_{\max}$  determined at the center of the joint for several values of  $\frac{d_A}{\tau c_A}$  and  $\frac{l_{\text{trans}}}{l_{\text{joint}}}$ . Results are postprocessed from the linear elastodynamic simulations. a)  $\frac{d_A}{\tau c_A} = 0.14$ , b)  $\frac{d_A}{\tau c_A} = 0.2$ , c)  $\frac{d_A}{\tau c_A} = 0.25$ , d)  $\frac{d_A}{\tau c_A} = 0.31$ , e)  $\frac{d_A}{\tau c_A} = 0.37$ , and f)  $\frac{l_{\text{trans}}}{l_{\text{joint}}} = \frac{11}{3}$ .

$$\frac{\sigma_{yy}^{\text{interface}}(t = \tau + \frac{d_A}{c_A})}{P_{\max}} \rightarrow 2 \quad \text{as} \quad \frac{Z_A}{Z_B} \rightarrow 0 \quad (7)$$

which tends to twice the applied pressure in the asymptotic limit where the acoustic impedance of the layer A is far lower than that of the layer B.

The optimal solution of the auxiliary optimization problem ( $p_1$ ) may considerably simplify that of ( $p_0$ ) (1). Especially, the condition (5) of localization of the tensile stress at the interface and its time of appearance  $t = \tau + \frac{d_A}{c_A}$  do remain valid. However, the validity of the optimal condition (6) becomes now questionable, and the optimal solution (7) remains an asymptotic ideal case. However, in practice, transverse effects of wave propagation tend to decrease the optimal solution. The objective of the present work is therefore to study the influence of those transverse effects on the maximum tensile stress actually reached at the interface, while taking advantage of some elements of the one-dimensional optimal solution which are transferable to the analysis of the two-dimensional case. Especially, another reduced array of unknowns relative to the “transverse” problem is considered

$$\mathbf{X}_T = \{d_A, l_{\text{trans}}\} \quad (8)$$

which consists of the thickness of the first layer and the transverse length of the laminate. The occurrence of  $d_A$  in the array  $\mathbf{X}_T$  is here to check the validity of the optimal condition (6) in the two-dimensional setting. As a matter of fact, the analysis of the direct problem has become analytically more complex, its solution will then be performed via numerical simulations. The isothermal and linearized geometrical framework is considered for these numerical simulations. More precisely, two different modelings of the loading applied on the laminate of increasing complexity will be considered. The first one is simplified and allows to carry out a simple linear elastodynamic analysis. The second one accounts for a weak coupling between an eddy current analysis delivering the mechanical loading to a subsequent linear elastodynamic analysis.

## 2.3. Methods of Analysis

### 2.3.1. Two-Dimensional Linear Elastodynamic Analysis

First, a linear elastodynamic analysis is carried out considering a simplified modeling of the magnetic pulse. Indeed, since the current discharged in the coil usually behaves as a damped sinusoid, the mechanical loading resulting from the magnetic pulse can be approximated by an applied pressure evolving as an exponentially decreasing square sine signal ([28] Equation (3)). For the sake of simplicity, only the first half pseudo-period of this signal will be considered in this study since it is its most significant part, as done in the study of Lagain et al. [31] The following pressure signal

$$\bar{P}(t) = \begin{cases} P_{\max} \sin^2\left(\frac{\pi t}{\tau}\right) & \forall t \in [0, \tau] \\ 0 & \text{otherwise} \end{cases} \quad (9)$$

is thus considered in Figure 4, with the values  $P_{\max} = 2.858$  MPa and  $\tau = 14.75$   $\mu\text{s}$ . The loading time  $\tau = \frac{\sqrt{LC}}{\pi}$  can be linked to the

inductance  $L$  and the capacitance  $C$  of the electrical circuit, and  $P_{\max}$  is the pressure related to the maximum intensity  $I_{\max}$  reached during the electrical discharge. The mechanical pulse (9) is applied uniformly on the subpart  $x \in [0, l_{\text{load}}]$  of the top face of the laminate ( $y = d_A + d_B$ ), as shown in Figure 5. Subsequent numerical simulations will be performed with a fixed value of the ratio  $\frac{l_{\text{load}}}{l_{\text{joint}}}$ . Its determination is detailed in Remark 1, at the end of Section 2. As a first step, this simplified modeling of the mechanical loading allows to study the effects of the sole wave propagation in the transverse direction, in a decoupled manner from any electromagnetic effects.

### 2.3.2. Weakly Coupled Two-Dimensional Eddy Current-Linear Elastodynamic Analysis

Next, electromagnetic effects are considered in the definition of the mechanical loading. An inductor of geometry of translation along the out-of-plane direction and of rectangular cross-section is thus considered, as shown in Figure 6, through which a current is discharged following a damped sine

$$I(t) = I_0 e^{-t/\tau_I} \sin(\omega t) \quad (10)$$

which is plotted in Figure 7, with  $I_0 = 1$  GA,  $\tau_I = 20$   $\mu\text{s}$  is the decay time, and  $\omega = \frac{\pi}{\tau} \simeq 213,000$   $\text{s}^{-1}$  is the angular frequency. A 1 mm air gap is set between the inductor and the top of the laminate. However, this standoff distance is not a key point in the present analysis because the optimization rather pertains here to the normal tensile stress ratio  $\frac{\sigma_{yy}^{\text{interface}}}{P_{\max}}$  at the interface, and not to  $\frac{P_{\max}}{I_{\max}}$ . Moreover, it can be shown that it does not influence the cross-sectional wave-propagation pattern, see Remark 2 for more details on this point.

The electromagnetic analysis is performed with an eddy-current formulation, [34] i.e., neglecting displacements currents, and more precisely using a formulation in potentials involving the electric scalar potential  $V$  and the magnetic vector potential  $A$ . Numerical simulation was performed with the finite element

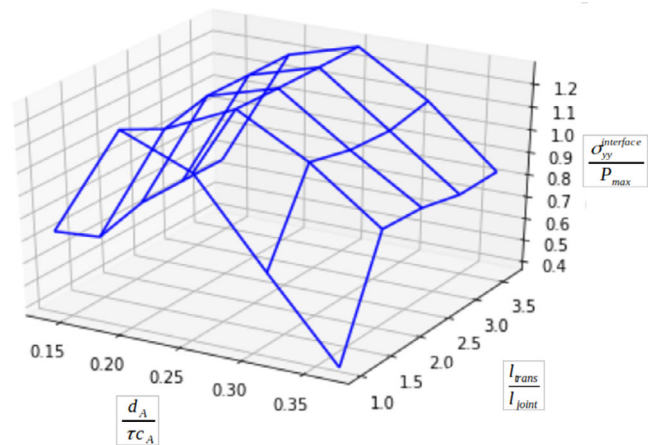


**Figure 11.** Maximal interfacial stress ratio  $\frac{\sigma_{yy}^{\text{interface}}}{P_{\max}}$  evaluated at the joint center, plotted as a function of  $\frac{l_{\text{trans}}}{l_{\text{joint}}}$  and  $\frac{d_A}{\tau c_A}$ .

software COMSOL Multiphysics.<sup>[32]</sup> The inductor and the laminate shown in Figure 6 are plunged into a large air box, with a vanishing magnetic vector potential at its boundary, except for the symmetry plane for which its normal gradient component vanishes. From the solution of the eddy-current analysis, Lorentz forces are computed from induced current flowing on the top face of the laminate. These forces are then used as input data for a subsequent linear elastodynamic analysis, hence defining a one-way or weak coupling between the two physics.

## 2.4. Computational Aspects

The computational domain (see Figure 5) is meshed with triangular P1 finite elements. The mesh is refined in an area  $(x, \gamma) \in [0, l_{load}] \times [0, d_A + d_B]$ . In this subarea, the mesh size varies between  $4 \times 10^{-2}$  mm at the top and bottom of the laminate as well as in the joint center, and up to  $5 \times 10^{-3}$  mm close to the right joint extremity. Derefinement is thus applied when departing from the joint area, as well as in the air, so that the mesh size reaches 8 mm at the boundary of the air box.

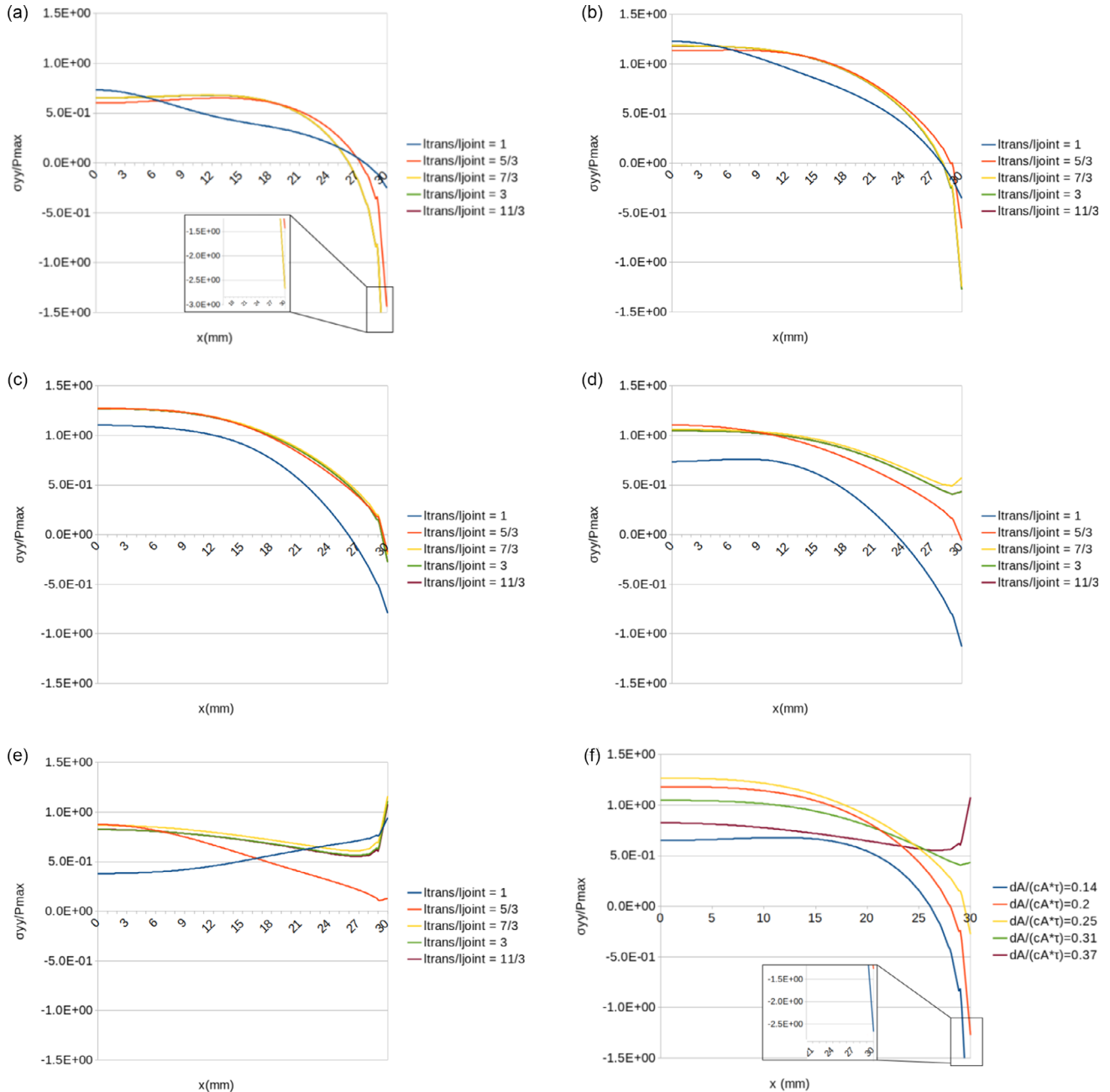


**Figure 12.** Profile of the interfacial stress ratio  $\sigma_{yy}/P_{max}$  plotted along the joint at the time when the stress is maximal for several values of  $\frac{d_A}{\tau_{cA}}$  and  $\frac{l_{trans}}{l_{joint}}$ . Results are postprocessed from the linear elastodynamic simulations. a)  $\frac{d_A}{\tau_{cA}} = 0.14$ , b)  $\frac{d_A}{\tau_{cA}} = 0.2$ , c)  $\frac{d_A}{\tau_{cA}} = 0.25$ , d)  $\frac{d_A}{\tau_{cA}} = 0.31$ , e)  $\frac{d_A}{\tau_{cA}} = 0.37$ , and f)  $\frac{l_{trans}}{l_{joint}} = \frac{11}{3}$ .



For eddy-current analysis, the inductor and the air gap, as shown in Figure 6, are meshed with the same refined mesh sizes. Next, the extremity of the joint can be viewed at first as a crack tip, which makes the problem singular. However, the present analysis rather aims at qualifying the effects of wave propagation in the transverse direction of the laminate to quantify the interfacial tensile stress rather than focusing on such singularity. Besides, from the experimental viewpoint such singularity does not really exist since the joint results from an assembly process. Therefore a fictitious radius of leave of  $5 \times 10^{-2}$  mm is introduced at the extremity of the joint to avoid the numerical results to be too much affected by that (fictitious) singularity, as illustrated in Figure 8.

A time-implicit generalized alpha method and a MUMPS solver are used for the solution of the eddy-current problem, while an explicit central difference time scheme is used to solve the linear elastodynamic equations with a step time of  $8 \times 10^{-8}$  s.

### 3. Two-Dimensional Linear Elastodynamic Numerical Results

#### 3.1. Stress Field in the Cross-Section of the Laminate

Figure 9 shows the map of the normal stress  $\sigma_{yy}$  in the cross-section of the laminate at time  $t = T = \tau + \frac{d_A}{c_A}$ , computed for the optimal configuration given by Equation (5) and (6), the latter being obtained from the one-dimensional analytical analysis. As expected, the tensile stress is maximal at the interface, and especially at the center of the joint ( $x = 0$ ). Next, the normal stress varies along the joint, ranging from tension at the center to compression at its extremity.

#### 3.2. Time Evolution of the Normal Stress Component $\sigma_{yy}$ at the Center of the Joint

A parametric analysis of the interfacial stress ratio  $\frac{\sigma_{yy}^{\text{interface}}}{P_{\text{max}}}$  is then carried out as a function of the variables  $X_T$  (8) of the optimization problem. More precisely, the normal stress  $\sigma_{yy}$  is extracted at the center of the joint ( $x = 0$ ) to provide comparable results with those given by the one-dimensional analytical analysis.

Figure 10 shows the time evolution of the interfacial stress ratio for various values of the ratio  $\frac{d_A}{\tau c_A}$  and of the transverse length ratio  $\frac{l_{\text{trans}}}{l_{\text{joint}}}$ . Let us precise that the ratio  $\frac{d_A}{\tau c_A}$  appears as the ratio of two lengths, and represents the ratio between the thickness of layer A to the distance that would be travelled by a pressure wave propagating in the medium A during the loading time  $\tau$ . This ratio was found convenient in the 1D analytical analysis to show the various regimes of debondability of the laminate, see Figure 7 of ref. [31]. In particular, the combination of Equation (5) and (6) yields an optimal value of this ratio of  $\frac{1}{4}$ . Another way to interpret this quantity is to transfer it as a comparison between two durations, particularly the time required for a pressure wave to travel across the whole thickness of the layer A and the loading time  $\tau$ . It was shown in the study of Lagain et al.<sup>[31]</sup> that the value of this ratio is connected to the number of wave back and forth performed by a pressure wave in the layer A during the loading time

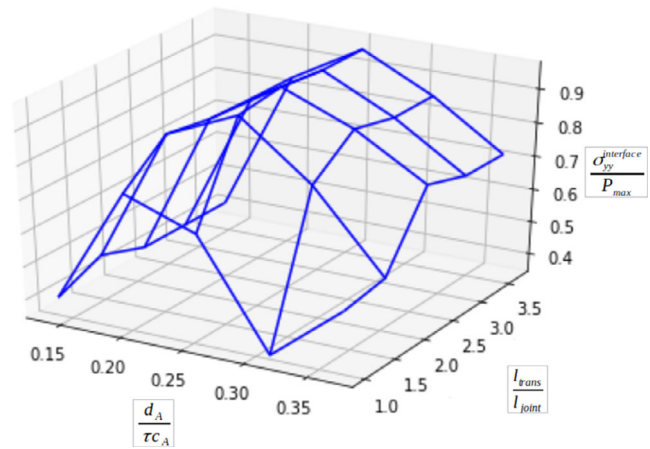


Figure 13. Maximal average of the interfacial stress ratio  $\frac{\sigma_{yy}^{\text{interface}}}{P_{\text{max}}}$  computed over the joint length, plotted as a function of  $\frac{l_{\text{trans}}}{l_{\text{joint}}}$  and  $\frac{d_A}{\tau c_A}$ .

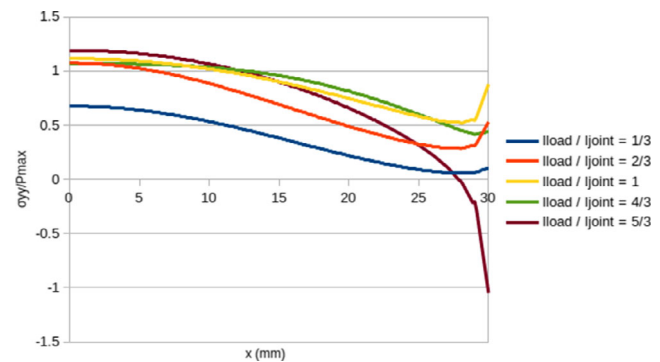


Figure 14. Profile of the interfacial stress ratio plotted along the joint at time  $t = T$ , for various values of the ratio  $\frac{l_{\text{load}}}{l_{\text{joint}}}$ .

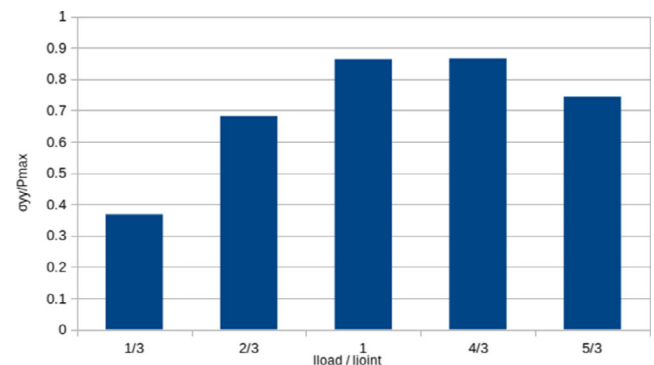


Figure 15. Averaged interfacial stress ratio computed over the joint length at time  $t = T$ , for various values of the ratio  $\frac{l_{\text{load}}}{l_{\text{joint}}}$ .

$\tau$  (see Table 1 of ref. [31]). However, it should be emphasized that in the present analysis, both the loading time  $\tau$  and material parameters of both layers are fixed, the former is involved in Equation (9), the latter are given in Table 1. Hence, only the thickness  $d_A$  is varied when varying the dimensionless ratio

$\frac{d_A}{\tau c_A}$  in Figure 10. The associated spanned values are  $d_A \in \{12, 17, 22, 27, 32\}$  mm. Similar remark can be noticed regarding the transverse ratio  $\frac{l_{\text{trans}}}{l_{\text{joint}}}$ . In particular, fixed values of  $l_{\text{joint}} = 30$  mm and of the ratio  $\frac{l_{\text{load}}}{l_{\text{joint}}} = \frac{4}{3}$  are set here, in such a way that varying the ratio  $\frac{l_{\text{trans}}}{l_{\text{joint}}}$  in Figure 10 amounts to only vary  $l_{\text{trans}} \in \{30, 50, 70, 90, 110\}$  mm since  $l_{\text{joint}}$  is fixed. More precisions are given in Remark 1 on required values of the ratio  $\frac{l_{\text{load}}}{l_{\text{joint}}}$ .

Figure 10a–e provides superposed time evolutions of the normal stress ratio at fixed  $\frac{d_A}{\tau c_A}$  for various values of  $\frac{l_{\text{trans}}}{l_{\text{joint}}}$ , while Figure 10f does the converse for  $\frac{l_{\text{trans}}}{l_{\text{joint}}} = \frac{11}{3}$ . Some comments are in order:

At fixed  $\frac{d_A}{\tau c_A}$ , the time evolutions of the interfacial stress ratio are superposed for values of the transversal length ratio  $\frac{l_{\text{trans}}}{l_{\text{joint}}}$  equal to  $\frac{7}{3}$ , 3 and  $\frac{11}{3}$ , from which it can be concluded that a transversal length ratio of  $\frac{7}{3}$  is sufficient to avoid any wave return from the lateral side of the laminate. In other words, in these cases the propagation of the wave in the  $x$  direction does not disturb the normal tensile stress at the center of the joint.

The configuration  $l_{\text{joint}} = l_{\text{trans}}$  (here illustrated by the instance  $\frac{l_{\text{trans}}}{l_{\text{joint}}} = 1$ ) corresponds to a laminate structure where the layers are bonded on all their surface. The debonding behavior of these structures is different because the maximal interface tensile stress ratio occurs at the second peak contrary to other configurations for which the first one is always the highest. For small values of the ratio  $\frac{d_A}{\tau c_A}$  (0.14 and 0.2), it can be seen that the second peak of the configuration  $\frac{l_{\text{trans}}}{l_{\text{joint}}} = 1$  is the highest, even higher than the first peak reached with configurations defined with other values of  $\frac{l_{\text{trans}}}{l_{\text{joint}}}$ .

At fixed value of the transversal length ratio  $\frac{l_{\text{trans}}}{l_{\text{joint}}}$ , the optimal condition (6) is retrieved numerically, yielding the highest interfacial stress ratio. As already said, this condition corresponds here to  $\frac{d_A}{\tau c_A} = \frac{1}{4}$ .

The thicker the first layer, the later the tensile stress occurs at the interface. This follows from the fact that the pressure wave travels along a longer distance.

Figure 11 shows the evolution of the maximal interfacial stress ratio as a function of the geometrical configuration of the

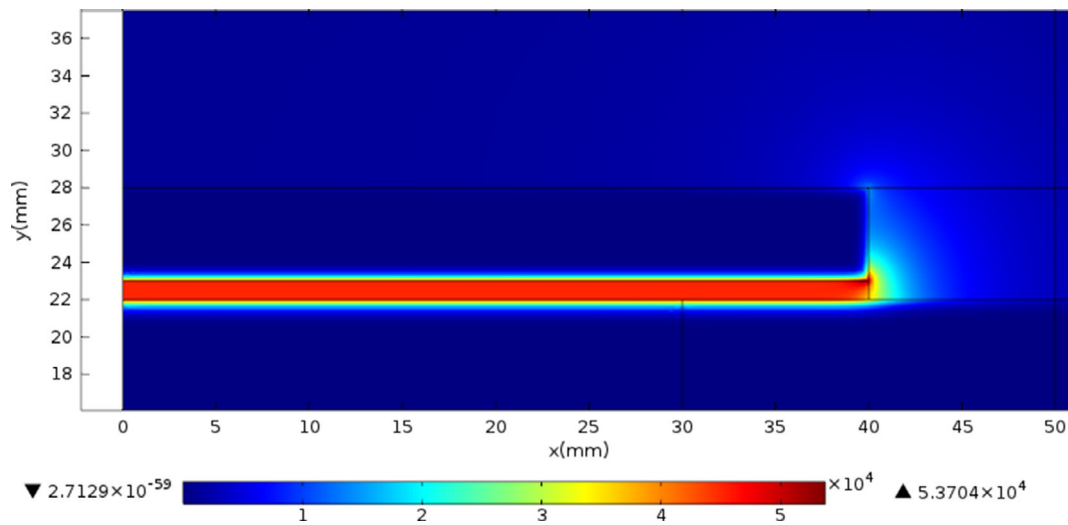


Figure 16. Magnitude of the magnetic field ( $\text{Am}^{-1}$ ) at time  $t = 10 \mu\text{s}$ .

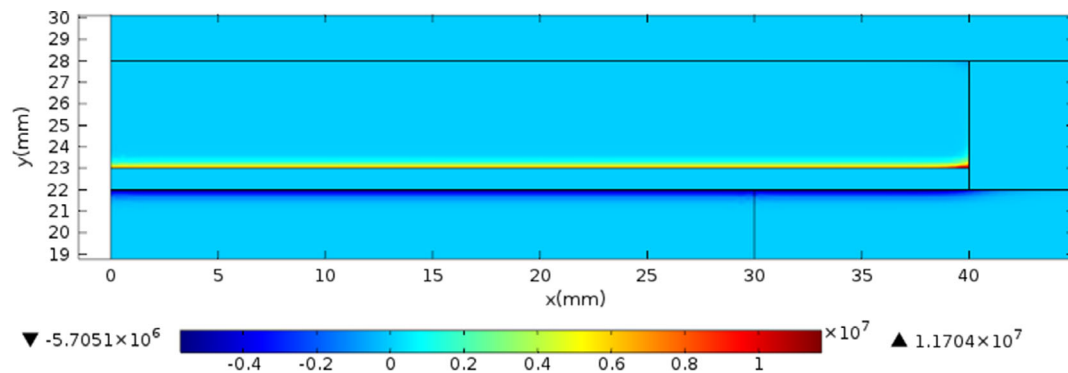
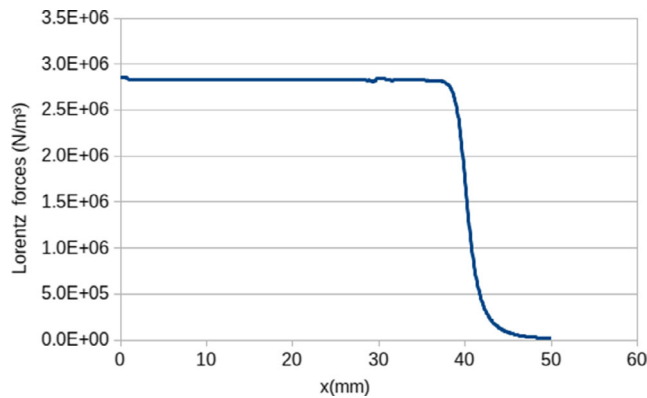
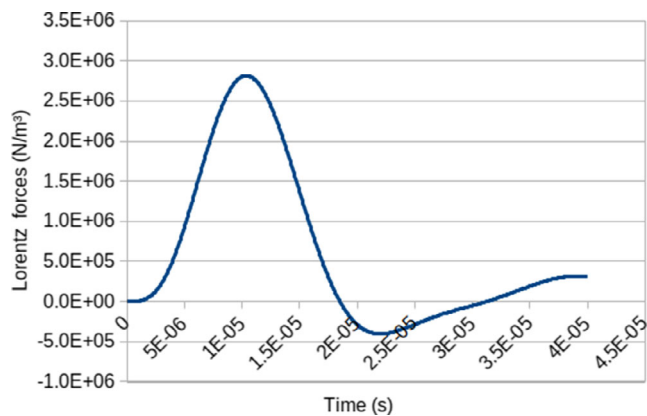


Figure 17.  $y$ -component of Lorentz forces ( $\text{Nm}^{-3}$ ) at time  $t = 10 \mu\text{s}$ .



**Figure 18.** Profile of the  $y$ -component of Lorentz forces plotted on the top face of the laminate at time  $t = 10 \mu\text{s}$ .



**Figure 19.** Time evolution of the  $y$ -component of Lorentz forces at the center of the top surface of the laminate.

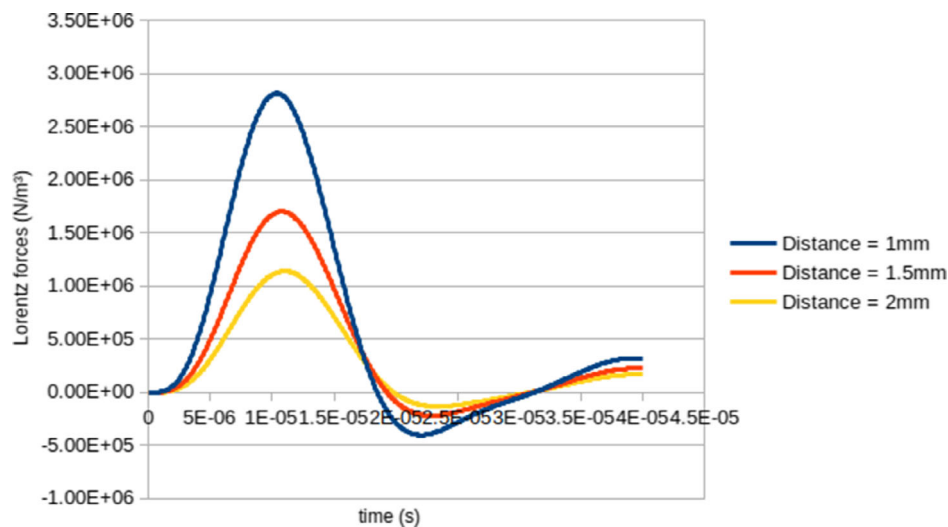


**Figure 20.** Profile of the  $y$ -component of Lorentz forces, plotted on the top face of the laminate at time  $t = 10 \mu\text{s}$ , for various distances between the inductor and the laminate.

laminates:  $\frac{\sigma_{yy}^{\max}}{P_{\max}} \left( \frac{h_{\text{trans}}}{h_{\text{joint}}}, \frac{d_A}{\tau c_A} \right)$ . It shows that the optimal configurations are in the region  $\frac{d_A}{\tau c_A} \in [0.2, 0.31]$  and  $\frac{h_{\text{trans}}}{h_{\text{joint}}} \in \left[ \frac{5}{3}, \frac{11}{3} \right]$ . It should be noticed that the stress ratios considered do not necessarily appear at the same time, because of the various values of the thickness of the layer A. These are the highest on the considered time range. Finally, for  $\frac{h_{\text{joint}}}{h_{\text{trans}}} = 1$ , the maximal interfacial stress ratio appears for  $\frac{d_A}{\tau c_A} = 0.2$ , but with a value which is still lower than the one obtained for the configurations  $\frac{h_{\text{trans}}}{h_{\text{joint}}} \in \left[ \frac{5}{3}, \frac{11}{3} \right]$  and  $\frac{d_A}{\tau c_A} = \frac{1}{4}$ .

### 3.3. Stress Distribution along the Joint at the Time When the Stress Is Maximal

**Figure 12** shows the profile of the interfacial normal stress ratio  $\frac{\sigma_{yy}^{\text{interface}}}{P_{\max}}$  along the joint at the time when it is maximal, plotted for several values of the geometric parameters  $\frac{d_A}{\tau c_A}$  and  $\frac{h_{\text{trans}}}{h_{\text{joint}}}$ . Particularly, this time is given for  $t = T$  for all configurations, except those given by  $\frac{h_{\text{trans}}}{h_{\text{joint}}} = 1$  and  $\frac{d_A}{\tau c_A} = 0.14$  or  $0.2$ , for which the higher interfacial stress ratio is reached at the second peak as mentioned above. Several observations can be made. First, the singularity of the problem at the joint extremity, although smoothed, points out some stress concentration as expected. Given the applied loading (9), the normal stress  $\sigma_{yy}$  oscillates between tension and compression in time at the joint extremity. However for the various values considered for the parameters  $\frac{d_A}{\tau c_A}$  and  $\frac{h_{\text{trans}}}{h_{\text{joint}}}$ , either tension (opening) or compression (closing) normal stress may occur at the joint extremity at the disassembly time. More precisely, **Figure 12** shows that there exists a threshold value of  $\frac{d_A}{\tau c_A} \approx 0.2$  below which compression occurs at the joint extremity, and above which tension appears at least for sufficiently large values of  $\frac{h_{\text{trans}}}{h_{\text{joint}}}$ . **Figure 12f** also shows that the best

interfacial stress ratio is achieved for values of the geometric parameters yielding a compressive normal stress at the joint extremity, while a tension one goes with a quite lower stress ratio (see  $\frac{d_A}{rc_A} = 0.37$  for instance). However, the simplicity the proposed modeling may not allow to conclude on the best configuration to disassemble, even though one may expect some non-linear effects to occur at the joint extremity and we are tempted to stick to the maximum interfacial stress ratio achieved at the joint center. Second, the optimality conditions (5) and (6) found by the one-dimensional analytical analysis are retrieved numerically in the two-dimensional setting, which corresponds here to the case  $\frac{d_A}{rc_A} = \frac{1}{4}$ .

In a complementary way to Figure 11, **Figure 13** shows the evolution of the maximal average of the interfacial stress ratio computed along the joint, as a function of the geometrical parameters  $\frac{d_A}{rc_A}$  and  $\frac{l_{trans}}{l_{joint}}$ . As in Figure 11, the optimal zone is shown to be  $\frac{d_A}{rc_A} \in [0.2, 0.31]$  and  $\frac{l_{trans}}{l_{joint}} \in [\frac{5}{3}, \frac{11}{3}]$ . Contrary to Figure 11, Figure 13 does not show any value of  $\frac{d_A}{rc_A}$  where the transversal length ratio  $\frac{l_{joint}}{l_{trans}} = 1$  is the best.

**Remark 1:** The geometrical ratio  $\frac{l_{load}}{l_{joint}}$ , fixed at  $\frac{4}{3}$  in this work, may have an influence on the achieved maximal tensile stress ratio. **Figure 14** and **15** respectively show the profile of the interfacial stress ratio and its averaged value computed over the joint length at time  $t = T$ , for various values of  $\frac{l_{load}}{l_{joint}}$ . Results shown in

these figures are obtained for  $(\frac{d_A}{rc_A} = 0.31, \frac{l_{trans}}{l_{joint}} = \frac{11}{3})$  (the brown curve shown in Figure 12d, almost superposed with the green one), with  $l_{joint} = 30$  mm as previously. Note that these values lead to that  $l_{trans}$  is here fixed at its highest value of 110 mm, to decorrelate the analysis of the geometrical ratio  $\frac{l_{load}}{l_{joint}}$  from the lateral dimension of the laminate  $l_{trans}$ , so that no wave return from the lateral side is expected to influence results shown in Figure 14 and 15.

Figure 15 shows that the averaged interfacial stress ratio computed over the joint length, when evaluated as a function of the geometrical ratio  $\frac{l_{load}}{l_{joint}}$ , appears as resulting from two antagonist effects in competition. First, for values of this geometrical ratio smaller than unity, the magnitude of the stress ratio appears far from its optimal value identified in the previous one-dimensional analytical analysis,<sup>[31]</sup> as shown in Figure 14 and 15. Second, as this geometrical ratio becomes greater than unity, although the stress ratio continues increasing in a monotonic manner at the joint center with  $\frac{l_{load}}{l_{joint}}$ , it becomes negative close to the joint extremity, so that the stencil where the joint is in tension is reduced. As a consequence, the averaged interfacial stress ratio shown in Figure 15 starts decreasing for  $\frac{l_{load}}{l_{joint}} = \frac{5}{3}$ . Hence, it appears a sort of optimal value for that geometrical ratio, balancing these two antagonist effects, of about  $\frac{4}{3}$ , which is the value retained in this work.

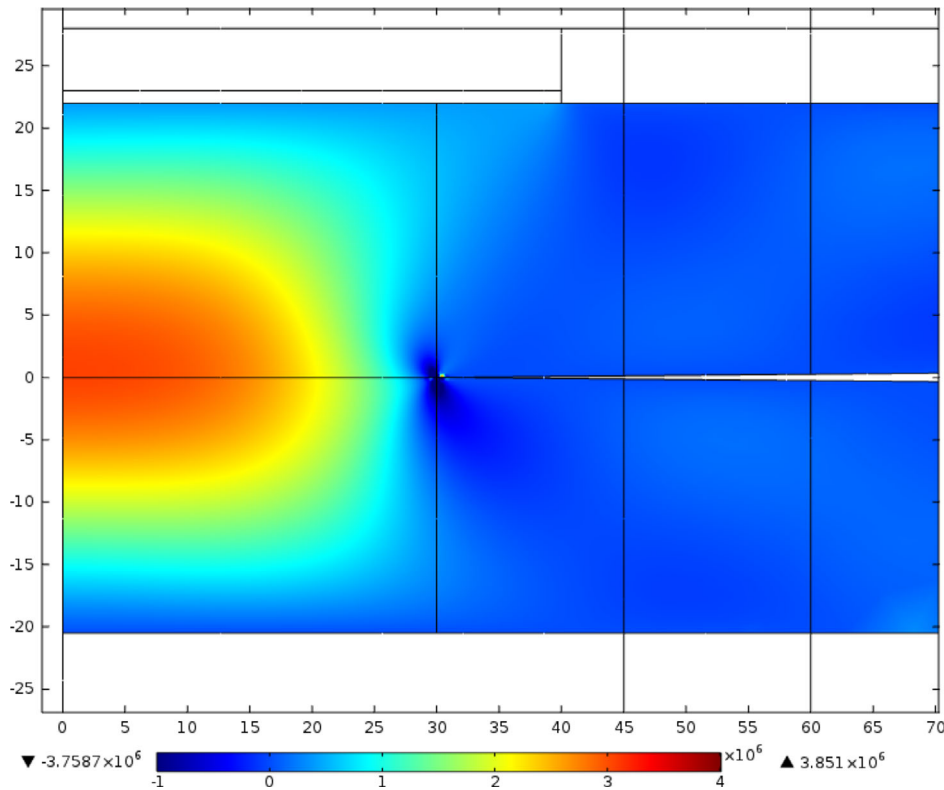


**Figure 21.** Map of the normal stress component  $\sigma_{yy}$  (in Pa) in the cross-section of the laminate at time  $t = T$ , when computed with the weakly coupled eddy current-linear elastodynamic analysis.

## 4. Two-Dimensional Eddy-Current Electromagnetic Coupled Linear Elastodynamic Numerical Results

### 4.1. Eddy-Current Electromagnetic Analysis

Since the inductor shown in Figure 6 is submitted to the prescribed current (10), a magnetic field is created between the inductor and the laminate, as shown in Figure 16. The induced time-varying magnetic flux density  $\mathbf{b}$  generates some eddy

current density  $\mathbf{j}$  in the skin of the top face of the laminate because the layer A is assumed to be electrically conductive. The skin depth within which eddy currents flow reads

$$\delta = \sqrt{\frac{2}{\omega \mu_0 \mu_r \kappa}} \quad (11)$$

where  $\omega$  is the angular frequency of the pulse,  $\mu_0$  and  $\mu_r$  are the magnetic permeability in vacuum and the relative permeability of

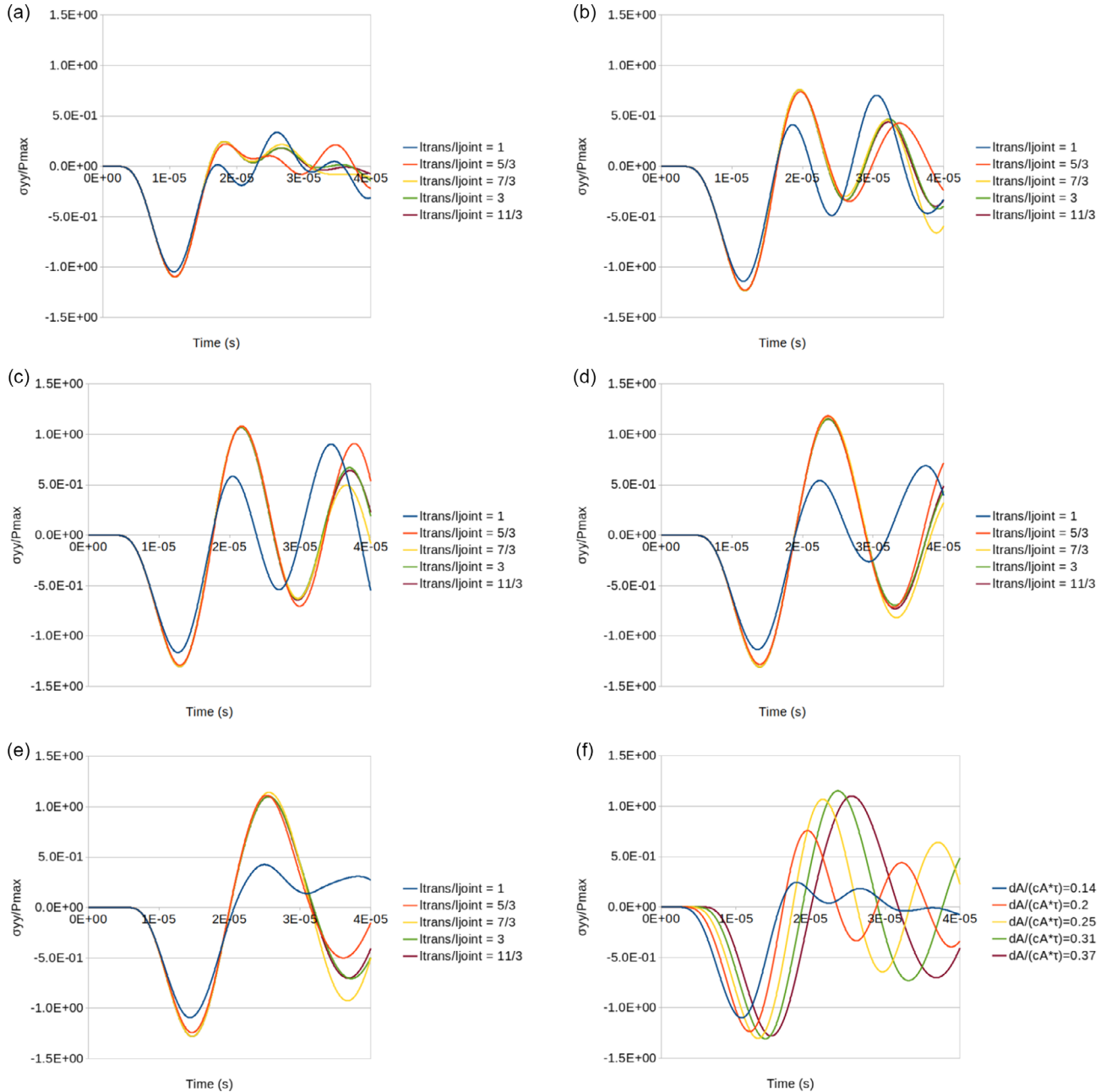


**Figure 22.** Time evolutions of the interfacial stress ratio  $\sigma_{yy}/P_{\max}$  extracted at the center of the joint for several values of  $\frac{d_A}{\tau c_A}$  and  $\frac{l_{\text{trans}}}{l_{\text{joint}}}$ . Results are post-processed from the weakly coupled eddy current-linear elastodynamic simulations. a)  $\frac{d_A}{\tau c_A} = 0.14$ , b)  $\frac{d_A}{\tau c_A} = 0.2$ , c)  $\frac{d_A}{\tau c_A} = 0.25$ , d)  $\frac{d_A}{\tau c_A} = 0.31$ , e)  $\frac{d_A}{\tau c_A} = 0.37$ , and f)  $\frac{l_{\text{trans}}}{l_{\text{joint}}} = \frac{11}{3}$ .

the material respectively, and  $\kappa$  denotes the electrical conductivity of the medium. Repulsive Lorentz body forces take place in this skin depth and result from the combination of the magnetic flux density  $\mathbf{b}$  and the current density  $\mathbf{j}$ , and are computed as

$$\mathbf{f} = \mathbf{j} \times \mathbf{b} \quad (12)$$

The map of the  $\gamma$ -component of Lorentz body forces is shown at its peak value in **Figure 17**, repulsing the laminate from the inductor. These body forces are distributed over a very thin depth. **Figure 5** shows the profile of  $\gamma$ -component of Lorentz forces plotted on the top face of the laminate. One can observe that they are almost uniformly distributed. Therefore, applying a uniformly distributed loading in the linear elastodynamic analysis as shown in **Figure 5** was a rather correct approximation. Besides, the time evolution of these Lorentz forces is shown in **Figure 19**. On the one hand, a force peak is observed at time  $t \approx 10 \mu\text{s}$  as expected, at which **Figure 16, 17, and 18** are plotted, and which more or less follows the square sine evolution (9) assumed in the linear elastodynamic analysis. On the other hand, a minimum appears at time  $t \approx 23 \mu\text{s}$ , arising from the fact that the imposed current (10) becomes negative during the second half of its pseudo-period. Electromagnetic effects thus result in this small negative peak of Lorentz forces shown in **Figure 19**, which was not considered in the previous purely mechanical analysis.

**Remark 2:** Regarding the location of the current source in the design of the magnetic pulse disassembly technology, the key point, here, is the time evolution of the induced mechanical loading, especially the duration of the pulse, rather than its amplitude. Indeed, on the one hand and due to the particular geometrical configuration of the inductor placed above the first layer of the laminate (see **Figure 6**), the time evolution of the mechanical loading generated at the top skin of this layer (actually Lorentz body forces) is independent of the distance between the inductor and the laminate, as shown in **Figure 20**. This distance only plays on the amplitude of the signal. On the other hand, taking advantage of the linearity of both the eddy-current and elastodynamic analyses, this amplitude plays no role in the study of cross-sectional effects on wave-propagation. Hence, this distance parameter should not enter the array of unknowns (8) of the optimization problem.

#### 4.2. Stress Map in the Cross-Section of the Laminate

**Figure 21** shows the map of the normal stress  $\sigma_{yy}$  in the cross-section of the laminate at the disassembly time  $t = T$ , for a configuration similar to that described in Section 2.1. Similar results are obtained with respect to **Figure 9**: the interfacial tensile stress is maximal at the center of the joint and decreases with the coordinate  $x$ , until being reversed to compression at the extremity of the joint (at  $x = 30 \text{ mm}$ ).

#### 4.3. Time Evolution of the Normal Stress Component $\sigma_{yy}$ at the Center of the Joint

As in Section 2, the time evolution of the interfacial stress ratio computed at the center of the joint is plotted in **Figure 22** for the

same geometric configurations of the laminate as in Section 2.2. The differences occurring with respect to Section 2.2 mainly result from the different time evolutions of the respective loadings, see **Figure 19**, which may also depend on the characteristics of the generator used.

**Figure 22** shows that, as for the purely linear elastodynamic results presented in Section 2, and for a given width of the first layer, the time evolutions of the interfacial stress ratio are similar for values of the transversal length ratio  $\frac{l_{\text{trans}}}{l_{\text{joint}}}$  equal to  $\frac{7}{3}$ , 3 and  $\frac{11}{3}$ . A transversal length ratio of at least  $\frac{7}{3}$  is necessary to avoid a wave return due to cross-sectional effects before the occurrence of the interfacial tensile stress at the time when the stress is maximum. However, the response obtained with a transversal length ratio is  $\frac{5}{3}$  is very close to the ones whose ratio values are such that  $\frac{l_{\text{trans}}}{l_{\text{joint}}} > \frac{7}{3}$ , and has a similar first peak. Furthermore, the same observations can be formulated about the configuration  $l_{\text{joint}} = l_{\text{trans}}$  than those already made in Section 2.

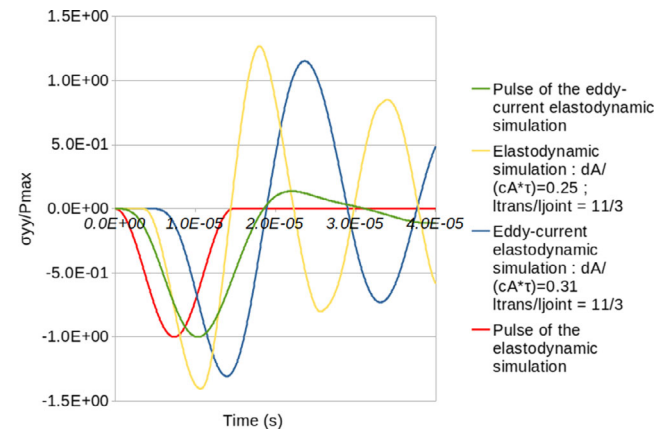


**Figure 23.** Time evolutions of the interfacial stress ratio  $\frac{\sigma_{yy}^{\text{interface}}}{P_{\text{max}}}$  computed at the center of the joint for the best configurations: comparison between linear elastodynamic and eddy-current coupled linear elastodynamic simulations.

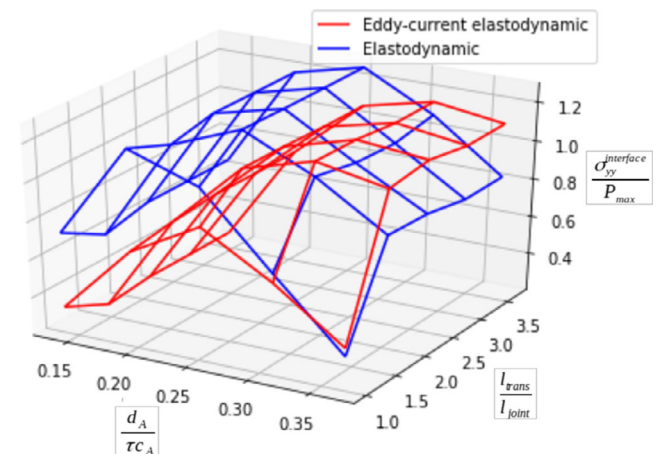


**Figure 24.** Comparison of the maximal interfacial stress ratio  $\frac{\sigma_{yy}^{\text{interface}}}{P_{\text{max}}}$  ( $\frac{l_{\text{trans}}}{l_{\text{joint}}}, \frac{d_A}{rc_A}$ ) computed at the joint center, with both linear elastodynamic and eddy-current coupled linear elastodynamic simulations.

One can also note that the highest tension peak is observed in Figure 22 for the configuration obtained with a width ratio of  $\frac{d_A}{\tau c_A} = 0.31$ , and not with that obtained for a width ratio of  $\frac{d_A}{\tau c_A} = \frac{1}{4}$  as concluded from Figure 10 and the one-dimensional analytical analysis.<sup>[31]</sup> However, the gap between the values of the maximum interfacial tensile stress obtained with values of the width ratio  $\frac{d_A}{\tau c_A} = \frac{1}{4}$ ,  $\frac{d_A}{\tau c_A} = 0.31$  and  $\frac{d_A}{\tau c_A} = 0.37$  is not really significant:

93% of the 0.31 configuration's stress for the 0.25 one and 95% for the 0.37 one.

Figure 23 shows a superposition of the time evolutions of the interfacial stress ratio  $\frac{\sigma_{yy}^{interface}}{P_{max}}$  extracted at the center of the joint and plotted for the best configurations deduced from the linear elastodynamic analysis ( $\frac{d_A}{\tau c_A} = \frac{1}{4}$ ) and from the eddy-current coupled linear elastodynamic simulation ( $\frac{d_A}{\tau c_A} = 0.31$ ). First, recall

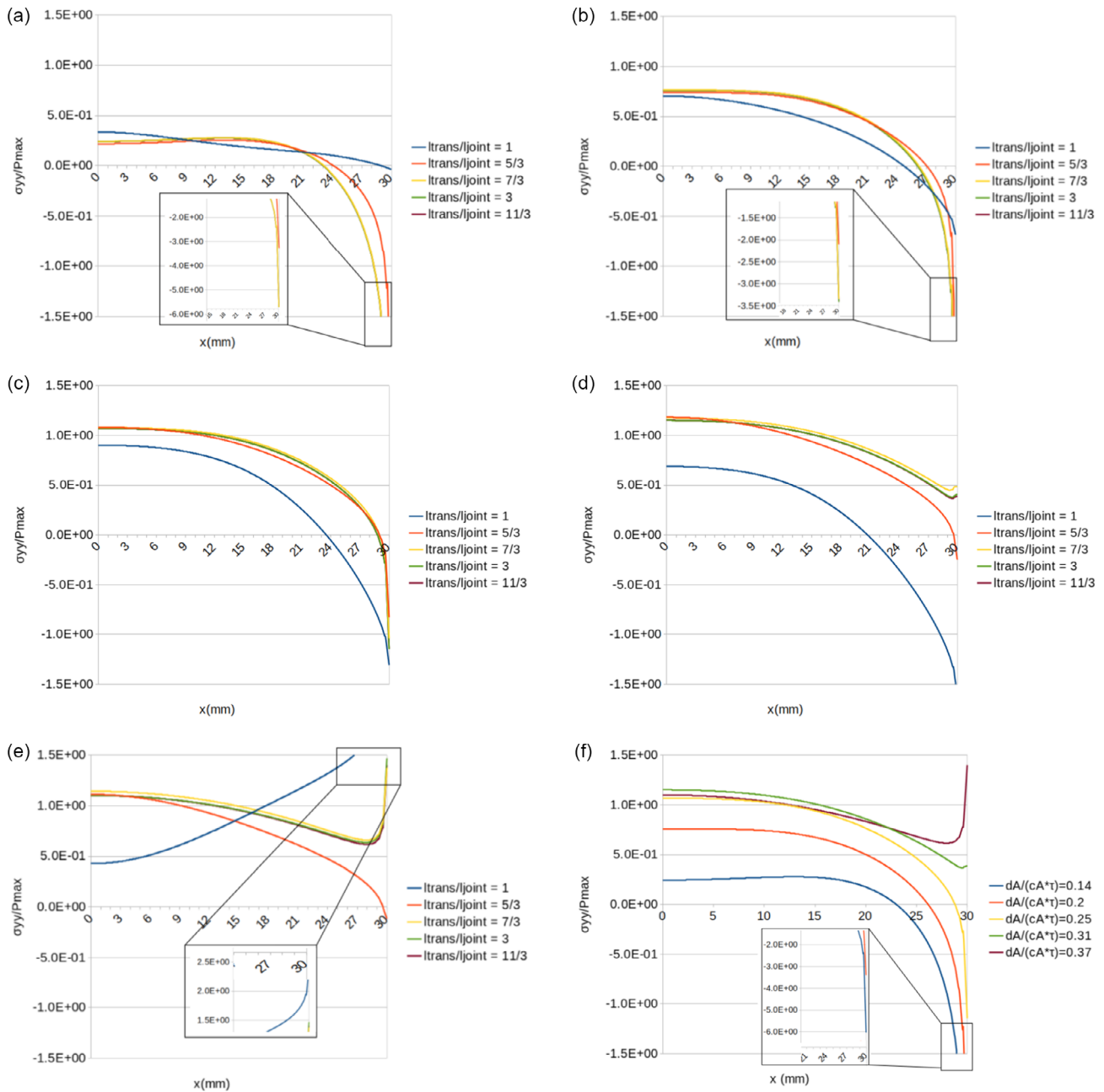


**Figure 25.** Profile of the interfacial stress ratio  $\sigma_{yy}/P_{max}$  plotted along the joint at the time when the stress is maximal for several values of  $\frac{d_A}{\tau c_A}$  and  $\frac{l_{trans}}{l_{joint}}$ . Results are postprocessed from the weakly coupled eddy current-linear elastodynamic simulations. a)  $\frac{d_A}{\tau c_A} = 0.14$ , b)  $\frac{d_A}{\tau c_A} = 0.2$ , c)  $\frac{d_A}{\tau c_A} = 0.25$ , d)  $\frac{d_A}{\tau c_A} = 0.31$ , e)  $\frac{d_A}{\tau c_A} = 0.37$ , and f)  $\frac{l_{trans}}{l_{joint}} = \frac{11}{3}$ .

that the two loading pulses look similar, except the occurrence of the second peak resulting from the eddy-current analysis. They have the same amplitude and a close duration (less than 15% difference). Second, the maximal interfacial stress ratio reaches 1.28 for the linear elastodynamic analysis, and 1.15 for the coupled one. According to the one-dimensional analytical analysis, the expected results computed for an aluminum/steel assembly were of 1.46 for  $\frac{d_A}{\tau c_A} = \frac{1}{4}$  and 1.37 for  $\frac{d_A}{\tau c_A} = 0.31$ . Therefore, 84% and 88% of the expected maximal interfacial tensile stress ratios are obtained numerically. Hence, although transverse effects lower the obtained optimal interfacial tensile stress ratios, the cross-sectional effects can be mitigated by choosing the relevant geometrical configurations.

**Figure 24** compares the maximal interfacial stress ratios computed with the two types of analyses, extracted at the center of joint, for various geometrical configurations of the laminate, i.e.,  $\frac{\sigma_{yy}^{interface}}{P_{max}} \left( \frac{l_{trans}}{l_{joint}}, \frac{d_A}{\tau c_A} \right)$ . It can be observed that the coupled analysis presents the existence of an optimal configuration in the range  $\frac{d_A}{\tau c_A} \in [0.25, 0.37]$  and  $\frac{l_{trans}}{l_{joint}} \in \left[ \frac{7}{3}, \frac{11}{3} \right]$ . The configuration  $\frac{l_{joint}}{l_{trans}} = 1$  is never the best one. Finally, results obtained with the coupled analysis always present smaller values of the interfacial tensile stress ratio than those obtained in linear elastodynamics, whatever the considered configuration.

#### 4.4. Stress Distribution along the Joint at the Time When the Stress Is Maximum

Similar to **Figure 12**, **Figure 25** shows the profile of the interfacial stress ratio along the joint at its maximum, computed with the coupled analysis for the same various geometrical configurations. It clearly appears here that the thicker the first layer, the higher the interfacial tensile stress ratio achieved in the main part of the joint length. Next, as the thickness of the first layer increases, the normal stress at the extremity of the joint tends to become a tensile one, as already mentioned in Section 2.3. A good compromise seems to be achieved with  $\frac{d_A}{\tau c_A} = 0.37$ , taking advantage of both an opening normal stress at the extremity, and a sufficiently high maximal interfacial stress ratio.

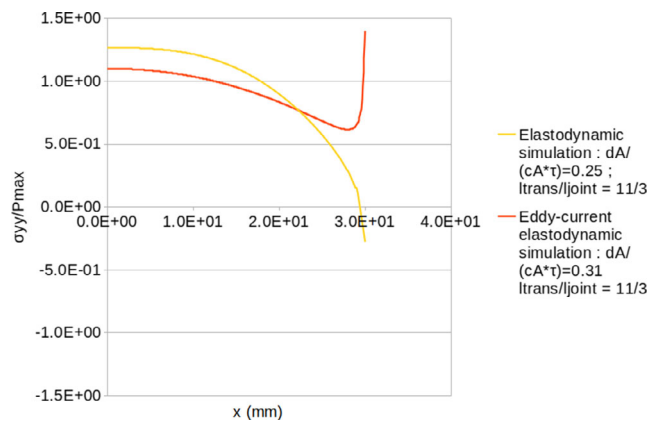


**Figure 26.** Profile of the interfacial stress ratio  $\sigma_{yy}/P_{max}$  plotted along the joint at time  $t = T$ , computed with both types of simulations for the respective best configurations.

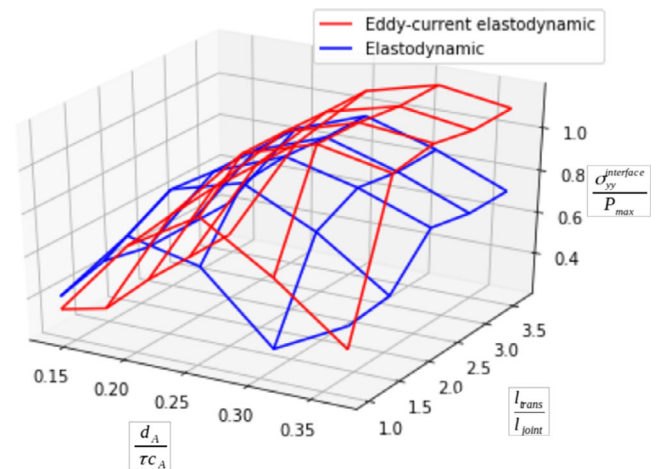


**Figure 27.** Comparison of the maximal average interfacial stress ratio  $\frac{\sigma_{yy}^{interface}}{P_{max}} \left( \frac{l_{trans}}{l_{joint}}, \frac{d_A}{\tau c_A} \right)$  computed over the joint length, when computed with both types of simulations.

**Figure 26** shows the profiles of the interfacial stress ratio plotted along the joint at time  $t = T$ , computed with both types of simulations for the respective best configurations. As already mentioned in Section 3.3, at the center of the joint, the best elastodynamic result predicts a value of the ratio 11% higher than the one computed with the coupled simulation. However in the latter, the stress concentration is a tensile one, the normal stress is therefore in tension in the whole joint length, so that both profiles cross each other at about 3/4 of the length of the joint. The latter seems therefore better for the disassembly.

Finally, **Figure 27** compares the maximal average of the interfacial stress ratio computed over the joint length, for the same geometrical configurations as in Section 2.2, and for both types of simulations. It can be seen that, for the eddy-current coupled linear elastodynamic simulation, the optimal configurations are the ones with  $\frac{d_A}{\tau c_A} > 0.31$  and  $\frac{l_{trans}}{l_{joint}} > 3$ . However, these results are strongly impacted by the stress concentration at the edge of the joint shown in **Figure 25**.

## 5. Conclusion

The objective of the present study was to make a further step in the design of the technology of magnetic pulse disassembly, to find an optimal geometric configuration allowing to disassemble dynamically a two-layered laminate involving a first electrically conductive layer. After a previous optimization step involving a one-dimensional analysis in the in-depth direction of the laminate,<sup>[31]</sup> the present work focused on the study of the influence of the effects of transverse wave propagation in the two-dimensional setting involving cross-sectional effects. To this end, numerical simulations resulting from two types of modeling, namely purely linear elastodynamics and eddy-current coupled linear elastodynamics, were carried out. They allowed to investigate numerically the domain of feasibility of an optimization problem with respect to two geometric variables: the thickness of the first layer, and the transverse dimension.



First, the linear elastodynamic simulations permitted to retrieve the optimal condition (6) found in the one-dimensional analytical analysis. When combined with a sufficiently long transverse length ratio ( $\frac{l_{\text{trans}}}{l_{\text{joint}}} = \frac{5}{3}$ ), a value of the interfacial stress ratio  $\frac{\sigma_{\text{interface}}}{P_{\text{max}}}$  of approximately 88% of the one predicted by the one-dimensional analytical solution was obtained. However, compression may occur at the extremity of the joint for the optimal configuration.

Next, the eddy-current simulation showed that the pulse is not a perfect square sine anymore, the optimal configuration thus changes to become the one with the thickest first layer (here  $\frac{d_A}{r_{cA}} = 0.37$ ). In this configuration, the interfacial tensile stress ratio computed at the center of the joint reached 1.37, which is  $\approx 84\%$  of the predicted one by the 1D analytical solution. Furthermore, in this configuration, the entire joint is subjected to a tensile normal stress at time  $t = T$ .

To sum up, the optimal geometrical configuration of a two-layered laminate structure to be disassembled by the magnetic pulse technology has to verify the two conditions (5) and (6) determined from the one-dimensional analysis, supplemented with a transverse ratio  $\frac{l_{\text{trans}}}{l_{\text{joint}}} > 1.6$ . From these results, a subsequent experimental campaign will be conducted, which will serve as a proof of concept for the magnetic pulse disassembling method.

## Acknowledgements

B.L. is funded on the one hand by Agence de l'Innovation de Défense (AID) grant reference number 2021 65 0044, and on the other hand by Ecole Centrale de Nantes.

## Conflict of Interest

The authors declare no conflict of interest.

## Data Availability Statement

Research data are not shared.

## Keywords

cross-sectional effects, disassembly, finite element method, laminate structure, magnetic pulse

Received: May 17, 2023

Revised: July 23, 2023

Published online: August 17, 2023

- [1] C. Bolis, L. Berthe, M. Boustie, M. Arrigoni, S. Barradas, M. Jeandin, *J. Phys. D: Appl. Phys.* **2014**, *64*, 108.  
[2] R. Ecault, M. Boustie, L. Berthe, F. Touchard, L. Chocinski-Arnault, H. Voillaume, B. Campagne, *Int. J. Struct. Integr.* **2014**, *5*, 253.

- [3] E. Gay, L. Berthe, M. Boustie, M. Arrigoni, A. Johnston, R. Cole, J. Barroeta, E. Buzaud. presented at *Proc. of the 18th DYMAT Technical Meeting*, Strasbourg, France, **2010**.  
[4] G. Tahan, M. Arrigoni, P. Bidaud, L. Videau, D. Thévenet, *Opt. Laser Technol.* **2020**, *129*, 106224.  
[5] J. L. Vossen, in *Measurements of Film-Substrate Bond Strength by Laser Spallation*, ASTM International, West Conshohocken, PA **1978**.  
[6] T. de Resseguier, E. Lescoute, G. Morard, F. Guyot, *AIP Conf. Proc.* **2009**, *1195*, 1007.  
[7] M. A. Meyers, in *Dynamic Behavior of Materials*, John Wiley & Sons, Hoboken, NJ **1994**.  
[8] M. L. Su, J. N. Li, K. G. Liu, W. J. Qi, F. Weng, Y. B. Zhang, J. S. Li, *Vacuum* **2019**, *159*, 315.  
[9] M.-L. Su, J.-S. Li, W.-J. Qi, J.-N. Li, *Phys. Scr.* **2019**, *94*, 115703.  
[10] L. Wang, *Foundations of Stress Waves*, Elsevier, Amsterdam **2011**.  
[11] R. Ciardiello, L. Greco, M. Miranda, F. Di Sciuillo, L. Goglio, *J. Adv. Join. Process.* **2020**, *1*, 100010.  
[12] R. Créac'Hcadec, L. Sohier, C. Cellard, B. Gineste. *Int. J. Adhes. Adhes.* **2015**, *61*, 81.  
[13] G. Stamoulis, N. Carrère, J.-Y. Cognard, P. Davies, C. Badulescu, *Int. J. Adhes. Adhes.* **2016**, *66*, 147.  
[14] A. Voloshin, M. Arcan, *Exp. Mech.* **1980**, *20*, 280.  
[15] A. Voloshin, M. Arcan, *Fibre Sci. Technol.* **1980**, *13*, 125.  
[16] V. Gupta, A. S. Argon, D. M. Parks, J. A. Cornie, *J. Mech. Phys. Solids* **1992**, *40*, 141.  
[17] E. Gay, L. Berthe, M. Boustie, M. Arrigoni, M. Trombini, *Compos. B: Eng.* **2014**, *64*, 108.  
[18] C. Luminita, M. Arrigoni, L. Deleanu, M. Istrate, *Mater. Plast.* **2018**, *55*.  
[19] M. Boustie, J. P. Cuq-Lelandais, C. Bolis, L. Berthe, S. Barradas, M. Arrigoni, T. De Resseguier, M. Jeandin, *J. Phys. D: Appl. Phys.* **2007**, *40*, 7103.  
[20] E. Gay, L. Berthe, M. Boustie, M. Arrigoni, E. Buzaud, *J. Phys. D: Appl. Phys.* **2014**, *47*, 455303.  
[21] A. Ben-Artzy, A. Stern, N. Frage, V. Shribman, O. Sadot, *Int. J. Impact Eng.* **2010**, *37*, 397.  
[22] M. Hahn, C. Weddeling, J. Lueg-Althoff, A. E. Tekkaya, *J. Mater. Process. Technol.* **2016**, *230*, 131.  
[23] A. Kapil, A. Sharma, *J. Clean. Prod.* **2015**, *100*, 35.  
[24] J.-N. Li, J.-S. Li, W.-J. Qi, K.-G. Liu, *Vacuum* **2019**, *168*, 108812.  
[25] J. Li, R. N. Raoelison, T. Sapanathan, G. Racineux, M. Rachik, *Proc. Manuf.* **2019**, *29*, 337.  
[26] J. S. Li, R. N. Raoelison, T. Sapanathan, Y. L. Hou, M. Rachik, *Acta Mater.* **2020**, *195*, 404.  
[27] F. Bay, J. Alves, in *8th Int. Conf. on High Speed Forming*, **2018**.  
[28] V. Psyk, D. Risch, B. L. Kinsey, A. E. Tekkaya, M. Kleiner, *J. Mater. Process. Technol.* **2011**, *211*, 787.  
[29] C. T. Sow, G. Bazin, T. Heuzé, G. Racineux, *Int. J. Mater. Form.* **2020**, *13*, 423.  
[30] J. D. Thomas, N. Triantafyllidis, A. Vivek, G. S. Daehn, J. R. Bradley, *Int. J. Fract.* **2010**, *163*, 67.  
[31] B. Lagain, T. Heuzé, G. Racineux, M. Arrigoni, *Int. J. Solids Struct.* **2023**, *275*, 112290.  
[32] COMSOL Multiphysics, *Introduction to COMSOL Multiphysics*, COMSOL Multiphysics, Burlington, MA, 32 (accessed: Feb 2018).  
[33] K. Tserpes, A. Barroso-Caro, P. A. Carraro, V. C. Beber, I. Floros, W. Gamon, M. Kozlowski, F. Santandrea, M. Shahverdi, D. Skejic, C. Bedon, V. Rajčić, *J. Adhes. J. Adhes.* **2022**, *98*, 1855.  
[34] J.-M. Jin, in *The Finite Element Method in Electromagnetics*, John Wiley & Sons, Hoboken, NJ **2015**.